

$S(^1D_2)$ atomic orbital polarization in the photodissociation of OCS at 193 nm: Construction of the complete density matrix

Suk Kyoung Lee

Department of Chemistry, Wayne State University, Detroit, Michigan 48202 and Department of Chemistry, Stony Brook University, Stony Brook, New York 11794

Ruchira Silva and Shakera Thamanna

Department of Chemistry, Wayne State University, Detroit, Michigan 48202

Oleg S. Vasyutinskii

Ioffe Physico-Technical Institute, Russian Academy of Sciences, 194021 St. Petersburg, Russia

Arthur G. Suits^{a)}

Department of Chemistry, Wayne State University, Detroit, Michigan 48202 and Department of Chemistry, Stony Brook University, Stony Brook, New York 11794

(Received 28 July 2006; accepted 31 August 2006; published online 13 October 2006)

The absolute velocity-dependent alignment and orientation for $S(^1D_2)$ atoms from the photodissociation of OCS at 193 nm were measured using the dc slice imaging method. Three main peaks ascribed to specific groups of high rotational levels of CO in the vibrational ground state were found, with rotationally resolved rings in a fourth slow region ascribed to weak signals associated with excited vibrational states of CO. The observed speed-dependent β and polarization parameters support the interpretation that there are two main dissociation processes: a simultaneous two-surface (A' and A'') excitation and the initial single-surface (A') excitation followed by the nonadiabatic crossing to ground state. At 193 nm photodissociation, the nonadiabatic dissociation process is strongly enhanced relative to longer wavelengths. The angle- and speed-dependent $S(^1D_2)$ density matrix can be constructed including the higher order ($K=3,4$) contributions for the circularly polarized dissociation light. This was explicitly done for selected energies and angles. It was found in one case that the density matrix is sensitively affected by the rank 4 terms, suggesting that the higher order contributions should not be overlooked for an accurate picture of the dissociation dynamics in this system. © 2006 American Institute of Physics. [DOI: 10.1063/1.2357948]

I. INTRODUCTION

It has long been known that photofragments produced by dissociation with polarized light can themselves be polarized, and this polarization can provide valuable insight into the underlying dissociation dynamics.¹ Considerable effort in recent years has been devoted to studying polarization of atomic orbitals in photodissociation as a probe of excited state symmetries, coherent effects, and nonadiabatic processes.^{2–8} Ion imaging and related methods have emerged as a premier means of investigating these phenomena owing to their ability to probe the nature of the angular momentum polarization as a function of photofragment recoil direction. This recoil angle dependence of orbital polarization, an example of a “ $\mathbf{v}\cdot\mathbf{J}$ vector correlation,” can afford deep insight into the dissociation event by revealing the dynamics in the molecular frame.⁹ The angular momentum polarization can be conveniently expanded in terms of multipole moments, ρ_{KQ} of rank K and component Q . The zeroth order multipole moment corresponds to the photofragment differential cross section, while odd and even order multipole moments describe the orientation and alignment, respectively. These polarization effects are directly reflected in nonequilibrium

populations of magnetic sublevels m_j , which are the projection of total angular momentum \mathbf{J} onto the recoil axis. Orientation, which may be probed only with circularly polarized light, is reflected in the odd-rank polynomial description of the magnetic sublevel population, while alignment, probed with linearly or circularly polarized light, corresponds to the even-rank polynomial description of magnetic sublevel population.

In general, ranks $K=1$ and 2 are considered the major contribution to orientation and alignment, respectively, and contributions of higher state multipoles are often neglected, even though multipoles up to rank $K=2J$ exist and should be included for a complete analysis. However, the higher order terms can be avoided by selecting a suitable probe scheme which is sensitive to specific contributions to the total angular momentum polarization from each multipole moment,⁹ as will be discussed in more detail in Sec. III. A fully quantum mechanical treatment has been developed for the $K=1,2$ moments^{4,9} and this was recently extended to the rank $K=3$ and $K=4$ cases.^{10,11}

A significant recent advance in imaging probes of orbital polarization has been the development of slice imaging methods^{12–14} that allow the angular momentum polarization to be measured directly over a large spread of photofragment

^{a)}Electronic mail: asuits@chem.wayne.edu

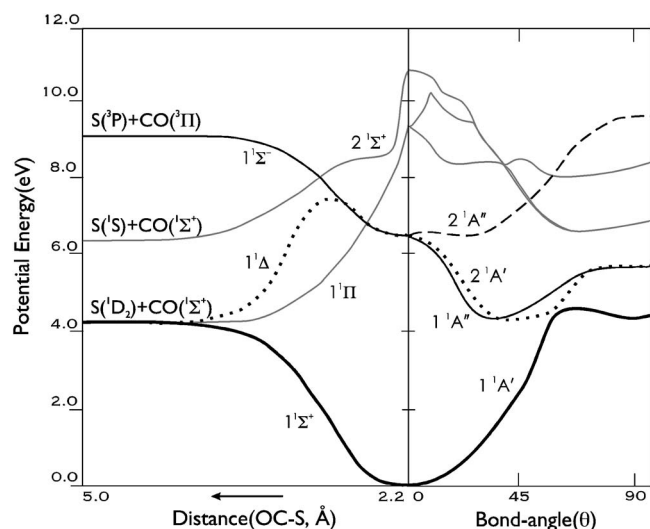


FIG. 1. Schematic diagram of the OCS potential curves as a function of the OC-S bond angle and internuclear distance adapted from Ref. 37.

recoil velocities, without needing to apply any form of forward convolution or inversion to the experimental data. Our previous applications of this approach in orbital polarization studies were to characterize alignment in the $S(^1D_2)$ photofragment from ethylene sulfide photodissociation¹⁵ and orientation of $O(^1D_2)$ in the ultraviolet photodissociation of ozone,¹⁶ both showing interesting recoil speed-dependent orbital polarization effects. For investigating the underlying photodissociation dynamics, most studies to date have focused on rank $K=2$ alignment [Cl_2 ,^{4,17} NO_2 ,¹⁸ N_2O ,¹⁹⁻²¹ $BrCl$,²² O_3 ,²³ OCS ,²⁴ HBr ,^{25,26} SO_2 (Ref. 27)] and rank $K=1$ orientation [ICl ,^{28,29} Cl_2 ,⁴ HCl ,³⁰ O_3 ,¹⁶ OCS ,^{24,31-33} $BrCl$ (Ref. 27)], ignoring the higher order moment contributions. However, the importance of the higher order $K=3,4$ terms is clear in some systems, such as O_3 , even though a quantitative analysis has not yet been performed.^{23,34} As mentioned above, theory has recently been extended to include the rank $K=4$ case for photofragment alignment and applied to the experimental case of $O(^1D_2)$ atoms from N_2O photodissociation¹¹ and the rank $K=3$ case for photofragment orientation applied to the experimental case of $Cl(^2P_{3/2})$ atoms from $BrCl$ photodissociation.¹⁰

Carbonyl sulfide (OCS) plays a key role in the atmospheric sulfur cycle,^{35,36} and it has been an attractive target for studies of photodissociation dynamics, as well as other isoelectronic molecules, CO_2 , N_2O , and CS_2 .³⁷⁻⁴⁴ For photodissociation in the 220–250 nm region, it is well known that the excitation from the ground state ($1^1\Sigma^+$) in the linear geometry is forbidden, while excitation of bent OCS is allowed for a transition to the excited states $1^1\Delta$ and $1^1\Sigma^1$. The former state becomes the $1^1A''$ state and the latter state splits into the $2^1A'$ and $2^1A''$ states in the bent geometry. These potential curves are illustrated schematically in Fig. 1. Suzuki *et al.*³⁷ reported that the excitations to the $2^1A'$ (parallel transition) and $1A''$ (perpendicular transition) states are involved in the main dissociation processes via conical intersections with A' and $A''(^1\Pi)$ states, ultimately leading to rotationally hot $CO(X^1\Sigma^+, \nu=0, J)+S(^1D_2)$ asymptotic products. They also attributed the slow S photofragments of a

bimodal energy distribution to nonadiabatic crossing between the $2^1A'$ and the $1^1A'$ ($1^1\Sigma^+$) ground state. The photodissociation of OCS in the vacuum ultraviolet has also been examined, where more excited states are accessible, such as $(1^1\Pi \leftarrow 1^1\Sigma^+)$ and $(2^1\Sigma^+ \leftarrow 1^1\Sigma^+)$ transitions at ~ 166.7 and ~ 152.7 nm, respectively.^{42,43} At 157 nm, the dominant channel is $S(^1S)+CO(^1\Sigma^+)$, yielding vibrational resolved angular and energy distributions of CO fragments.⁴³

Most previous studies of atomic orbital orientation and alignment have been carried out for OCS around 230 nm.^{24,31-33} Recently, van den Brom *et al.* investigated orbital orientation of $S(^1D_2)$ photofragment produced from state-selected OCS ($\nu_2=0,1|JM$), observing the dependence of orientation on bending excitation at 230 nm.³² They suggested that the contribution of the molecular frame polarization parameter $Im[a_1^{(1)}]$ (defined as γ_1' in our formalism) mainly comes from the simultaneous excitation to two potential surfaces ($2^1A'$ and $1^1A''$), resulting in the phase shift between the scattering wave functions. Important recent developments in understanding OCS photochemistry have come from the Janssen group, who used hexapole focusing to prepare laboratory frame oriented, state-selected parent OCS molecules for photodissociation studies. Their work has provided insight into deviations from axial recoil, an issue examined in some detail below.

In the following pages, we present a detailed slice imaging study of $S(^1D_2)$ orbital alignment and orientation in OCS photodissociation at 193 nm. The paper is organized as follows. Section II presents the experimental background, Sec. III details the theoretical approach for extracting quantitative alignment and orientation data from slice imaging measurements, Sec. IV shows the experimental data and anisotropy parameters, Sec. V provides interpretation and discussion, and finally, Sec. VI is devoted to the conclusions.

II. EXPERIMENT

The overall experimental setup employed in the dc slice imaging approach has been described in detail elsewhere^{13,15} and only the points specific to this particular study will be given here. A brief experimental schematic diagram and the coordinate system used for analyzing the data are shown in Fig. 2. A pulsed supersonic molecular beam of OCS seeded 10% in Ar was expanded into the source chamber and collimated by a skimmer. The beam entered into a velocity mapping electrode assembly optimized for dc slice imaging and was intersected at right angles by two counterpropagating laser beams. The photolysis laser light (193 nm) was generated by an ArF excimer system running at 30 Hz (GAM EX10/300). In order to produce the linearly polarized light, the laser output was first allowed to propagate through a total of eight fused silica windows set at Brewster's angle before being focused into the interaction region using a 40 cm lens. Control over the polarization was achieved using Berek's compensator (New Focus) for cases where circular polarization

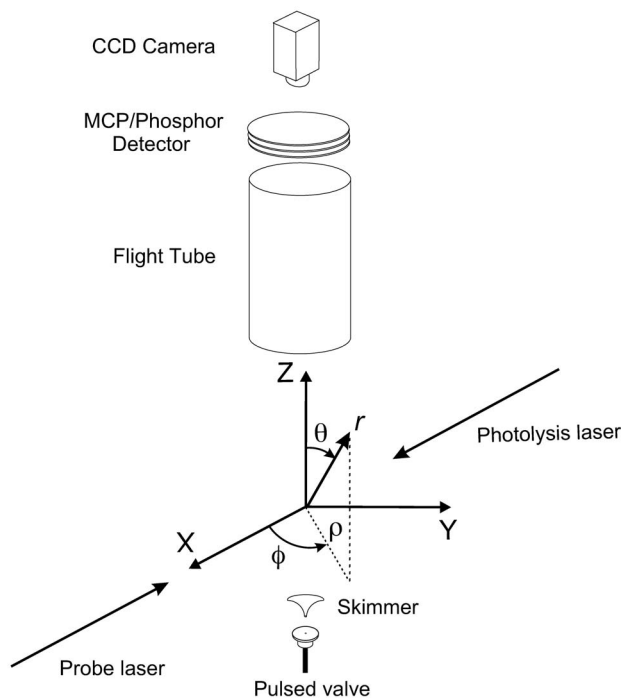
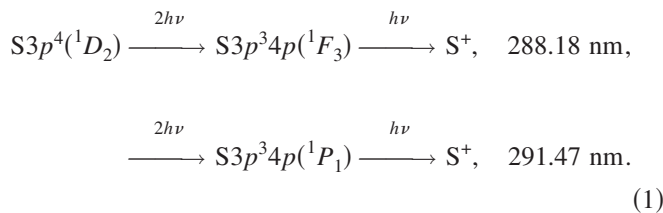


FIG. 2. Schematic experimental setup and laboratory frame coordinate system.

was required. The photolysis laser power was approximately 0.5 mJ/pulse. The probe laser was provided by frequency doubling the output of a dye laser (rhodamine 610/590 dyes) pumped by the 532 nm harmonic of a second Nd:yttrium aluminum garnet (YAG) laser (Quanta Ray PRO 290). A magnesium fluoride Soleil-Babinet compensator (Karl Lambrecht) was used to produce the required circular polarization. The probe beam (~ 3 mJ/pulse) was then focused through a second 30 cm lens. The $S(^1D_2)$ atomic photofragments produced in the dissociation event were probed using the following two (2+1) resonance enhanced multiphoton ionization (REMPI) schemes:



As mentioned previously, since each REMPI probe transition has its own sensitivity to the various multipole moment contributions to the orbital polarization of the photofragments, the higher order moments can be obtained selectively using the above two schemes. This will be considered more deeply in the following section. Following ionization, the S ions were accelerated through the multilens velocity mapping assembly and impacted upon a dual micro-channel plate array of 75 mm diameter, which was coupled to a P-47 phosphor screen. In this particular instance a repeller electrode held at +700 V was used in conjunction with three additional focusing lenses in the velocity mapping scheme to stretch the photofragment ion cloud along the

time-of-flight axis to around 350 ns. The overall flight path from the laser interaction region to the detector was 100 cm. Application of a narrow (~ 40 ns) time gate at the detector was then used to sample the central section of the distribution. The resulting image was recorded using a charge coupled device (CCD) camera (Sony XC-ST50, 768×494 pixels) in conjunction with the IMACQ megapixel acquisition program⁴⁵ recently developed in our group that enabled a high-resolution real time ion counting. A fully detailed description of this approach may be found in our previous work.^{13,45}

III. THEORY

The coordinate system we use in our analysis of the angular distribution of photofragment state multipoles is displayed in Fig. 2.^{4,9} The state multipoles, ρ_{KQ} with ranks $K = 0 \cdots 2J$ and projections $Q = -K \cdots K$, are expressed in terms of a series of anisotropy polarization parameters, which are associated with different dynamical mechanisms taking place during the dissociation processes. In this study, multipoles up to $K=4$ can exist. The zeroth-rank state multipole ρ_{00} is proportional to the total population and the multipoles with rank $K>0$ describe the anisotropy of the photofragment angular momenta.

The absorption of polarized probe light by photofragments via a two-photon transition can be expressed in terms of the state multipoles that are a function of polar (θ) and azimuthal (ϕ) angles of the photofragment recoil direction vector.^{46,47} Usually, the spatial modulations in an ion image which result from photofragment orientation and alignment represent a relatively small fraction of the total signal. For this reason, it is useful to isolate these contributions by taking linear combinations of the signal recorded under different experimental geometries of the photolysis and probe laser polarizations in such a way that the population term ρ_{00} cancels. Specifically, for the case of probing photofragment alignment, the following combination of signals can be used for isolating the rank $K=2,4$ state multipoles from the population and orientation terms:

$$\begin{aligned}
 &\frac{I_Z(\theta, \phi) - I_Y(\theta, \phi)}{\langle I_X \rangle + \langle I_Y \rangle + \langle I_Z \rangle} \\
 &= \frac{\sqrt{2j_i + 1}}{2} \left[\frac{P_2}{P_0} \left\{ \rho_{20} + \frac{\sqrt{6}}{3} \text{Re}[\rho_{22}] \right\} \right. \\
 &\quad \left. + \frac{P_4}{12P_0} \{ 5\rho_{40} - 2\sqrt{10} \text{Re}[\rho_{42}] - \sqrt{70} \text{Re}[\rho_{44}] \} \right], \tag{2}
 \end{aligned}$$

where $I_Y(\theta, \phi)$ and $I_Z(\theta, \phi)$ are absorption intensities related to linearly polarized probe light with polarization vectors directed along the Y and Z axes, respectively. The probe light is assumed to propagate along the $-X$ axis. The extraction of photofragment orientation can be achieved by the linear

TABLE I. Line strength factors of two different 2+1 REMPI transitions by circularly and linearly polarized light.

Circular	1F_3	1P_1	Linear	1F_3	1P_1
P_1^c/P_0	0	-1.181	P_2/P_0	0.683	-0.598
P_3^c/P_0	-0.253	0	P_4/P_0	-0.115	-1.069

combination of ion images recorded with right and left circularly polarized probe light. The relevant expressions may be found in the previous discussion, Eq. (3.4) of Ref. 16. The P_K terms above are the line strength factors which, in the case of a (2+1) REMPI probe scheme, may be evaluated with the simple expression given by Mo and Suzuki.⁴⁸ The line strength factors which are relevant to the $^1D_2 \rightarrow ^1F_3$ and $^1D_2 \rightarrow ^1P_1$ two-photon REMPI transitions in sulfur atom are presented in Table I. It is seen from Table I that the $^1D_2 \rightarrow ^1F_3$ transition is sensitive only to the $K=3$ state multipole, while the $^1D_2 \rightarrow ^1P_1$ transition is sensitive only to the $K=1$ state multipole. Therefore, the contribution of the $K=1$ and $K=3$ state multipoles to the experimental signal can be determined independently. It is more difficult to extract the rank 4 contribution because, although the sensitivity of the 1P_1 is about ten times higher than that of 1F_3 , the line strength factors are nonzero for each of the two transitions. Recent work of Smolin *et al.* has shown a way to isolate the rank 4 moments from all others experimentally.¹¹ However, in this particular instance, it is convenient to obtain the $K=4$ moments by fitting to the experimental image obtained via the 1P_1 transition using the fixed values of the $K=2$ moments measured via the 1F_3 transition in which they are clearly isolated.

The denominator on the left hand side of Eq. (2) is a normalization factor which is proportional to the total population of all fragment magnetic sublevels,⁹ $\langle \rho_{00}(\theta, \phi) \rangle$, and the angular brackets denote averaging of the corresponding absorption intensities over all recoil angles. As discussed in more detail in our previous publication,¹⁶ the slice imaging technique used in this study allows one to monitor only the narrow central part of the total three-dimensional absorption signal, which, in our coordinate scheme, corresponds to fixing θ to a value of $\pi/2$.¹⁵ The sliced image can be normalized by the zeroth-rank fragment state multipole $\rho_{00}(\theta, \phi)$

integrated over the azimuthal angle ϕ at fixed value of the polar angle $\theta = \pi/2$. In practice, the measurement of I_X in Eq. (2) may be impossible for the photolysis laser polarized along the Y -axis case (defined here as geometry II), which precludes proper normalization. However, when the polarization of the photolysis laser lies parallel to the Z -axis case (geometry I), this problem can be circumvented since the overall photofragment distribution will exhibit equal sensitivity to both X - and Y -axis probe light polarizations. That is, the total signal intensity of I_X is same as that of I_Y . Taking this fact into account, the alignment anisotropy parameters, such as η_2 and $s_2 + \alpha_2$, were measured for the geometry I case [see Eq. (3)] and used to normalize the data for the geometry II case. The experimental results from the geometry I setup were not used exclusively, because they do not give us γ_2 and independent s_2 and α_2 parameters. An alternative way to normalize the data for the geometry II case is to use the normalization factor shown as the denominator in Eqs. (5) and (6). In this case, the geometry I experiment would be unnecessary. The denominator in Eqs. (5) and (6) is also proportional to the total intensity (i.e., the sliced population term), however, which has an experimental advantage over that used in Eqs. (2)–(4). Since the determination of fragment population for any fragment spatial distribution can be carried out by changing only the probe laser polarization without moving the laser beam direction,⁹ this would be a more direct alternative method for normalizing the measurements. However, in the present work some of these measurements were not available. Substituting the state multipoles for the case of sliced images into Eq. (2), the explicit expressions to obtain alignment (geometries I and II) and orientation (geometries III and IV) are given below.

Geometry I. The photolysis light is linearly polarized along the Z axis:

$$\begin{aligned}
 & \frac{I_Z(\pi/2, \phi) - I_Y(\pi/2, \phi)}{\langle I_X(\pi/2, \phi) \rangle + \langle I_Y(\pi/2, \phi) \rangle + \langle I_Z(\pi/2, \phi) \rangle} \\
 &= \frac{1}{(1 - \beta/2)} \left[\frac{C' P_2}{2 P_0} \left\{ (s_2 + \alpha_2)(\cos 2\phi - 1) - \frac{1}{2} \eta_2(3 + \cos 2\phi) \right\} \right. \\
 & \quad \left. + \frac{C'' P_4}{12 P_0} \{ 5(s_4 + \alpha_4)(3 + 4 \cos 2\phi - 7 \cos 4\phi) + \sqrt{15} \eta_4(5 + 4 \cos 2\phi + 7 \cos 4\phi) \} \right]. \quad (3)
 \end{aligned}$$

Geometry II. The photolysis light is linearly polarized along the Y axis:

$$\begin{aligned}
& \frac{I_Z(\pi/2, \phi) - I_Y(\pi/2, \phi)}{\langle I_X(\pi/2, \phi) \rangle + \langle I_Y(\pi/2, \phi) \rangle + \langle I_Z(\pi/2, \phi) \rangle} \\
&= \frac{1}{(1 + \beta/4)} \left[\frac{C' P_2}{2P_0} g \left\{ s_2(\cos 2\phi - 1) + \frac{\alpha_2}{2}(3 \cos^2 2\phi - 4 \cos 2\phi + 1) + \gamma_2 \sin^2 2\phi + \frac{\eta_2}{4}(\cos^2 2\phi + 4 \cos 2\phi + 3) \right\} \right. \\
&\quad + \frac{C'' P_4}{12P_0} \left\{ \frac{5}{2}(3 + 4 \cos 2\phi - 7 \cos 4\phi)(2s_4 + (3 \cos 2\phi - 1)\alpha_4) - 2\sqrt{30}\gamma_4(5 + 12 \cos 2\phi + 7 \cos 4\phi)\sin^2 \phi \right. \\
&\quad \left. \left. - \frac{\sqrt{15}}{4}\eta_4(14 + 25 \cos 2\phi + 18 \cos 4\phi + 7 \cos 6\phi) \right\} \right], \quad (4)
\end{aligned}$$

where

$$C' = \sqrt{5}V_2(j)/4\pi, \quad C'' = 3V_4(j)/32\pi,$$

$$V_2(j) = 5\{j(j+1)/[(2j+3)(2j-1)]\}^{1/2},$$

$$V_4(j) = 9\{(j(j+1))^3/[(j-1)(j+2)(2j-3)(2j-1)(2j+3)(2j+5)]\}^{1/2}.$$

Geometry III. The photolysis (right circularly polarized) and the probe light (right or left circularly polarized) propagate along the X and $-X$ axes, respectively:

$$\begin{aligned}
& \frac{I_R^X(\pi/2, \phi) - I_L^X(\pi/2, \phi)}{\langle I_Z(\pi/2, \phi) \rangle + \langle I_Y(\pi/2, \phi) \rangle - (1/3)[\langle I_R^X(\pi/2, \phi) \rangle + \langle I_L^X(\pi/2, \phi) \rangle]} \\
&= -\frac{3\sqrt{3}}{(1 - \beta/8)\pi} \left[\frac{P_1^c}{P_0} \left\{ \alpha_1 \cos^2 \phi + \frac{\gamma_1}{2} \sin^2 \phi \right\} + \frac{P_3^c}{P_0} \frac{\sqrt{7}V_3(j)}{2\sqrt{3}} \left\{ \alpha_3 \cos^2 \phi(5 \cos^2 \phi - 3) + \gamma_3 \frac{\sqrt{6}}{4} \sin^2 \phi(5 \cos^2 \phi - 1) \right\} \right]. \quad (5)
\end{aligned}$$

Geometry IV. The photolysis and the probe light counterpropagate along the X axis, with the photolysis light linearly polarized at 45° to the detector plane and the probe light circularly polarized:

$$\begin{aligned}
& \frac{I_R^X(\pi/2, \phi) - I_L^X(\pi/2, \phi)}{\langle I_Z(\pi/2, \phi) \rangle + \langle I_Y(\pi/2, \phi) \rangle - (1/3)[\langle I_R^X(\pi/2, \phi) \rangle + \langle I_L^X(\pi/2, \phi) \rangle]} \\
&= -\frac{3\sqrt{3}}{(1 - \beta/8)\pi} \frac{\sin^2 \phi}{2} \left[\frac{P_1^c}{P_0} \gamma'_1 + \frac{P_3^c}{P_0} \sqrt{14}V_3(j) \left\{ \frac{\gamma'_3}{4}(5 \cos^2 \phi - 1) + \eta_3 \cos^2 \phi \right\} \right], \quad (6)
\end{aligned}$$

where $V_3(j) = j(j+1)/[(j-1)(j+2)(2j-1)(2j+3)]^{1/2}$.

Alignment anisotropy parameters α_K , γ_K , and η_K for $K=2$ and 4 are defined in Refs. 49 and 11, respectively. Note that the factor $1/12$ in the term P_4/P_0 in Eq. (2) was accidentally omitted in Eqs. (13) and (14) in Ref. 11. The orientation anisotropy parameters α_K , γ_K , and η_K for $K=1$ and 3 are defined in Refs. 49 and 10, respectively.

The angular distribution of the orbital photofragment polarization in Eqs. (3) and (6) is defined in terms of the anisotropy parameters that, as mentioned above, characterize the extent to which a distinct physical mechanism plays a role in the overall dissociation dynamics. The alignment parameters in Eqs. (3) and (4), s_K , α_K , γ_K , and η_K with $K=2, 4$, describe contributions to the total alignment from incoherent and coherent excitations: s_K and α_K define incoherent excitation via both parallel and perpendicular transitions, with the limiting cases $s_K=2\alpha_K$ and $\alpha_K=-s_K$ representing pure perpendicular and pure parallel processes, respectively. The γ_K parameters correspond to alignment from a coherent

superposition of perpendicular and parallel excitations, while η_K parameters arise from a coherent superposition of two perpendicular transitions. Although it is not presented in the expressions above, the contribution from a coherent superposition of parallel and perpendicular excitations is characterized by γ'_K in the case of circularly polarized photolysis light (see Ref. 50). In our study, it is excluded due to the experimental difficulties in extracting this parameter. The rank 1 and 3 orientation parameters α_K and γ_K in Eq. (5) describe contributions to the fragment orientation from incoherent perpendicular excitation and a coherent superposition of a parallel and a perpendicular excitation, respectively. Both parameters arise from propagation of the photon helicity into photofragments. The parameter γ'_1 in Eq. (6) relates to a coherent superposition of a parallel and a perpendicular excitation that results from the transition dipole moment aligned to the photolysis light polarization vector \mathbf{e} .

The description of the angular momentum polarization in the molecular frame provides a useful connection to

theory. The molecular frame state multipoles normalized by the zeroth-rank state multipole can be easily obtained from the laboratory frame state multipoles using a rotation matrix. In the case of circularly polarized photolysis light, the molecular frame state multipoles can be expressed as the following equations.⁵¹ For ranks 1 and 3,

$$\rho_{K0}^{\text{mol}}(\Theta) = \sigma \frac{3\sqrt{2K+1}\alpha_K V_K(j)\cos\Theta}{\sqrt{2j_i+1}\left[1 - \frac{1}{2}\beta P_2(\cos\Theta)\right]}, \quad (7)$$

$$\begin{aligned} \rho_{K1}^{\text{mol}}(\Theta) = \sigma & \frac{3\sqrt{2K+1}\gamma_K V_K(j)\sin\Theta}{2\sqrt{2}\sqrt{2j_i+1}\left[1 - \frac{1}{2}\beta P_2(\cos\Theta)\right]} \\ & + \frac{3i\sqrt{2K+1}\gamma'_K V_K(j)\sin\Theta\cos\Theta}{2\sqrt{2}\sqrt{2j_i+1}\left[1 - \frac{1}{2}\beta P_2(\cos\Theta)\right]}, \end{aligned} \quad (8)$$

$$\rho_{32}^{\text{mol}}(\Theta) = \frac{3}{\sqrt{5}} \frac{\sqrt{2K+1}\eta_K V_K(j)\sin^2\Theta}{\sqrt{2j_i+1}\left[1 - \frac{1}{2}\beta P_2(\Theta)\right]}, \quad (9)$$

and for ranks 2 and 4,

$$\rho_{K0}^{\text{mol}}(\Theta) = \frac{\sqrt{2K+1}V_K(j)[s_K + \alpha_K P_2(\cos\Theta)]}{\sqrt{2j_i+1}\left[1 - \frac{1}{2}\beta P_2(\Theta)\right]}, \quad (10)$$

$$\begin{aligned} \rho_{K1}^{\text{mol}}(\Theta) = & \frac{\sqrt{6}\sqrt{2K+1}V_K(j)\gamma_K\sin\Theta\cos\Theta}{4\sqrt{2j_i+1}\left[1 - \frac{1}{2}\beta P_2(\cos\Theta)\right]} \\ & + \sigma \frac{\sqrt{6}i\sqrt{2K+1}V_K(j)\gamma'_K\sin\Theta}{4\sqrt{2j_i+1}\left[1 - \frac{1}{2}\beta P_2(\cos\Theta)\right]}, \end{aligned} \quad (11)$$

$$\rho_{K2}^{\text{mol}}(\Theta) = \frac{\sqrt{6}\sqrt{2K+1}V_K(j)\eta_K\sin^2\Theta}{8\sqrt{2j_i+1}\left[1 - \frac{1}{2}\beta P_2(\Theta)\right]}, \quad (12)$$

where Θ is the angle between the direction of light propagation and the recoil axis and the values of the index $\sigma = +1$ and $\sigma = -1$ correspond to the right and left light circular polarizations, respectively. It is clear from Eqs. (7)–(9) that the parameters α_K are responsible for the photofragment electronic angular momentum which is parallel to the recoil direction \mathbf{v} , while the parameters γ_K are responsible for the angular momentum which is perpendicular to the recoil direction and lies in the plane defined by the recoil vector \mathbf{v} and the propagation direction of the photolysis laser beam. The parameter γ'_1 is attributed to angular momentum perpendicular both to the recoil vector \mathbf{v} and to the photolysis light

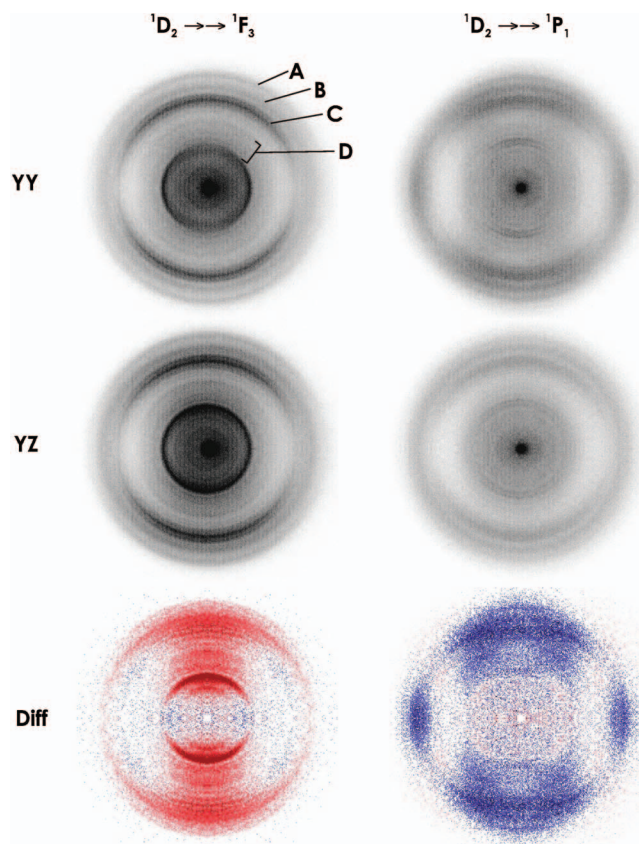


FIG. 3. (Color) dc sliced images and difference images of $S(^1D_2)$ in the photodissociation of OCS at 193 nm for indicated combination of photolysis-probe laser polarization. Red and blue correspond to positive and negative intensities, respectively.

polarization vector \mathbf{e} . All molecular frame state multipoles can be used to produce the electron charge cloud distribution^{20,52} and the full density matrix of the atomic fragment⁵² that are dependent on recoil direction, giving us information on the molecular frame dynamics.

IV. RESULTS

Experimental images obtained at a photolysis wavelength of 193 nm using two different REMPI transitions as a probing scheme are shown in Fig. 3. The Y -polarized dissociation laser (see Fig. 2) was used with both Z - and Y -polarized probe, which corresponds to the geometry II case (defined in Sec. III). For normalizing the data and improving measurement statistics, geometry I measurements (Z -polarized photolysis) were also performed but the results are not shown here.

The resulting images show features not seen in previous studies around 230 nm, and some of these are owing to the higher resolution of the slicing approach, but more importantly owing to the different photolysis energy. In the faster fragments, there are three distinct rings which are likely associated with some specific groups of rotational states of the CO cofragments, and these are labeled A–C. For the $^1D_2 \rightarrow ^1F_3$ REMPI probe transition, an intense inner ring comes from hot-band dissociation produced by the probe laser alone; this has been explicitly studied before.⁴⁴ Although we used a dilute sample to reduce this contribution, this sig-

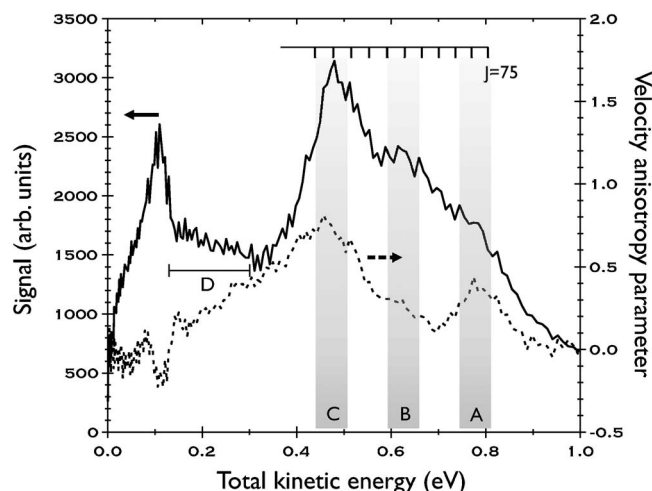


FIG. 4. Total translational energy distribution (solid line) and corresponding velocity anisotropy parameter β (dashed line). Shaded bars highlight peak regions for discussion (see text).

nal from the $\nu_2=2$ bending state of the OCS parent molecule always exists but was omitted from our analysis. On the other hand, there is little one-laser signal in the 1P_1 REMPI transition owing to the difference in wavelength. A comparison of the angular distributions of the experimental images for the two geometry cases confirms that the relatively weak signals lying right beyond the one-laser signal (labeled the *D* region) are due to S fragments from 193 nm dissociation. The *D* region consists of several rings corresponding to resolved rotational structure of CO cofragments. In particular, two distinct rings in the *YY* image with a probe wavelength at 291.47 nm (top right in Fig. 3) show an energy spacing of ~ 0.028 eV.

Figure 4 shows the total translational energy distribution and β parameter obtained from the *YY* image (top left in Fig. 3). The comb above shows the rotational levels for the CO cofragment in $v=0$ obtained using the dissociation energy $D_0=25\,311$ cm $^{-1}$, the excitation energy of $S(^1D_2)$, and the internal energy constants of CO ($\omega_0=2169.81$ cm $^{-1}$, rotational constants B_0 , D_0 from Ref. 40). The peak of the *A* ring is assigned to $J\approx 76$ of the CO cofragment in the ground vibrational level. The *B* and *C* rings are peaked at $J\approx 79$ and 84, respectively. The highest β parameter (≈ 0.8) was observed in the *C* ring, while for the *B* ring the smallest value was measured, $\beta\approx 0.3$, which is almost the same as that obtained in the *D* ring. The *A* region photofragments show a slightly larger β value (≈ 0.4) than those in the *B* ring.

The rank 2 and 4 alignment anisotropy parameters are extracted by fitting the difference images to the relevant equations, (3) and (4), including the correct normalization factor weighted by the recoil-dependent β for the sliced image. The fitting results are plotted as a function of S atom recoil speed in Fig. 5. The trend of s_2 and α_2 alignment parameters indicates that over the whole range, an incoherent parallel transition (characterized by $s_2\approx -\alpha_2$) is dominant but with a minor contribution from the perpendicular transition at some recoil regions. An interesting feature is the variation of the γ_2 parameter over the three rings, showing evidence that the dissociation dynamics in the *C* ring is dis-

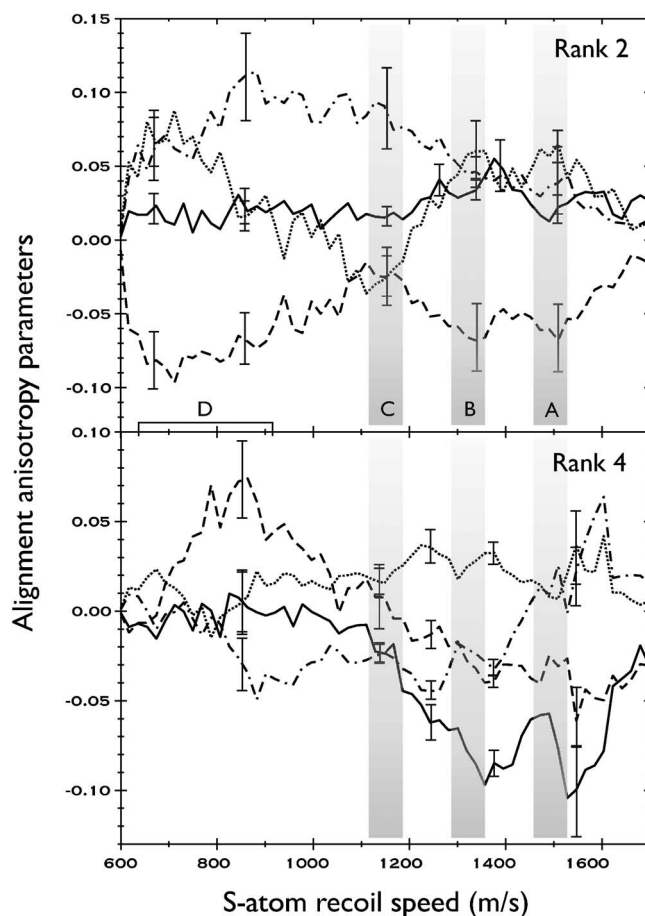


FIG. 5. Speed-dependent alignment anisotropy parameters for $O(^1D_2)$ from OCS at 193 nm arising from the following mechanisms: s_K (dashed line) and α_K (dot-dashed line) which both describe incoherent excitation, and γ_K (dotted line) and η_K (solid line) which correspond to coherent excitation (as discussed in the main text in detail). Three shadow bars denote the speed region where three distinct peaks are placed in images.

tinct from that in the other two rings. Comparing to the *A* and *B* rings, the fragments in the *C* ring have small negative γ_2 values representing a coherent parallel/perpendicular contribution. This strong recoil speed dependence of γ_2 indicates that two different dynamics are likely contributing. Even though the size of the effect is small, a contribution of coherent perpendicular excitation described by η_2 exists around the *B* ring and especially in the outer edge of the *A* ring. The η_4 contribution is quite strong in the same region. That means two perpendicular transitions are involved in those regions.

In order to determine the three orientation parameters (α_K , γ_K , and γ'_K), right and left circularly polarized probe light is used and the photolysis light is polarized either circularly or linearly at 45° with respect to the flight axis (*Z* axis). The difference images are seen in Fig. 6 for REMPI detection via the 1P_1 intermediate, which is only sensitive to the rank 1 orientation contribution. The alternate REMPI scheme was used to determine the rank 3 parameters, which were found to be negligible within the uncertainty of the measurement. The recoil speed-dependent rank 1 orientation parameters are plotted in Fig. 7. One striking feature is the γ'_1 contribution in the *B* ring arising from coherent parallel/perpendicular excitation. In addition to the dominant γ'_1 ori-

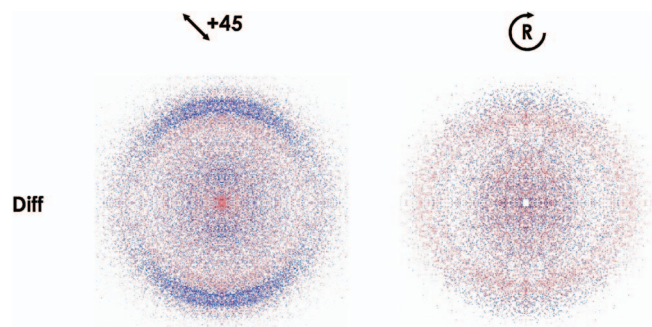


FIG. 6. (Color) dc sliced difference images for indicated combination of photolysis-probe laser polarization measured via the $^1D_2 \rightarrow ^1P_1$ REMPI transition. Red and blue correspond to positive and negative intensities, respectively.

entation, there are small effects for γ_1 and almost zero for α_1 . These are associated with transfer of the photon helicity into the photofragment. For nonlinear triatomic molecules, it has been suggested that the α_1 and γ_1 will typically be quenched in the dissociation process.¹⁶

V. DISCUSSION

The previous studies of OCS photodissociation around 230 nm show bimodal translational and angular distributions related to two different dissociation dynamics: the slow channel arising from nonadiabatic transition from the $2^1A'$ to the ground state ($1^1A'$) and the fast channel resulting from a simultaneous excitation to two excited states ($2^1A'$ and $1^1A''$). As expected, the slower fragments had a large value of β due to a nearly pure parallel transition of the A' state, while the faster one showed a small or near-zero value implying the contribution from a pure perpendicular transition to the $1^1A''$ state. This interpretation was also supported by wave packet calculation of Suzuki *et al.*, displaying three distinct rotational distributions corresponding to different dissociation mechanisms: one from nonadiabatic crossing to

the ground state from $2^1A'$, another from the adiabatic process along the $2^1A'$ state, and the third from the adiabatic process via the $1^1A''$ state.³⁷ However, the two adiabatic pathways were overlapped up in the experimental results at ~ 230 nm. These results from the longer wavelength photolysis can provide guidance to interpret the dissociation dynamics at 193 nm. First, the β value can give us the important clue on the symmetry of excited electronic states involved.

The large positive β in the C ring may indicate that the fragment is formed by dissociation from the A' excited state corresponding to a mostly parallel component of the transition dipole moment. On the other hand, the small β values in the B and A rings imply possibly that some perpendicular excitation is involved in those recoil speed regions, or there is greater bending in these regions. That is, the prominent lower value of β in the B ring may be ascribed to a multi-surface excitation in which the contribution of transition to A'' state (pure perpendicular) becomes significant. It should be pointed out here that although the A and B rings are attributed to the admixture of dissociation from two excited states, the contribution of the A'' state is larger in the B ring, accounting for the trend of the β parameter.

If the photolysis light is linearly polarized, the expression for the photofragment angular distribution $N(\Theta)$ can be presented in the following traditional form:⁵³

$$N(\Theta) = \sqrt{2j_A + 1} \rho_{00}(\Theta) = \frac{1}{4\pi} [1 + \beta P_2(\cos \Theta)], \quad (13)$$

where Θ is the angle between the light polarization vector \mathbf{e} and the recoil vector \mathbf{k} and $P_2(\cos \Theta)$ is the Legendre polynomial of the second order.

If the photolysis light is circularly polarized or unpolarized the result is

$$N(\Theta) = \frac{1}{4\pi} \left[1 - \frac{\beta}{2} P_2(\cos \Theta) \right], \quad (14)$$

where Θ is the angle between the direction of light propagation and the vector \mathbf{k} .

It has been known that the dissociation of OCS at 230 nm gives rise to nonaxial recoil dynamics, even though the β value of ~ 1.8 was observed at CO ($N=62$) fragment corresponding to the slow channel.⁵⁴ Recently, a quantum mechanical study of the nonaxial recoil problem was reported for the photodissociation of a diatomiclike molecule by Kuznetsov and Vasyutinskii using the quasiclassical approximation.⁵⁵ The main result of this work is that, neglecting Coriolis mixing, the rotation of the molecular axis during dissociation can be described by a number of rotation factors which depend on the rank of the incident photon polarization matrix, on dissociation mechanism, and on the classical angle of rotation of the recoil axis γ . Also, each experimentally determined anisotropy parameter of the rank $K \geq 0$ can be presented as product of the corresponding rotation factor and the “axial recoil” anisotropy parameter.

However, the result of Kuznetsov and Vasyutinskii cannot be directly applied to the photodissociation of a rapidly rotating planar triatomic molecule with the transition dipole

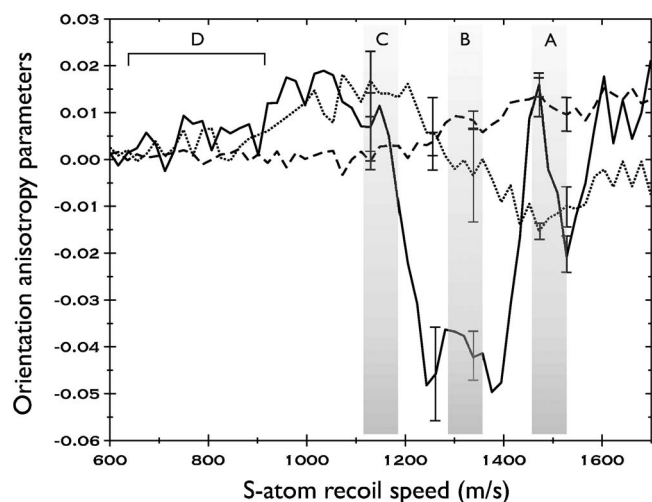


FIG. 7. Speed-dependent orientation anisotropy parameters for O(1D_2) from OCS at 193 nm arising from the following mechanisms: α_1 (dashed line) which represents incoherent perpendicular excitation, and γ_1 (dotted line) and γ'_1 (solid line) which describe coherent superposition parallel/perpendicular excitation. Three shadow bars denote the speed region where three distinct peaks are observed in the images.

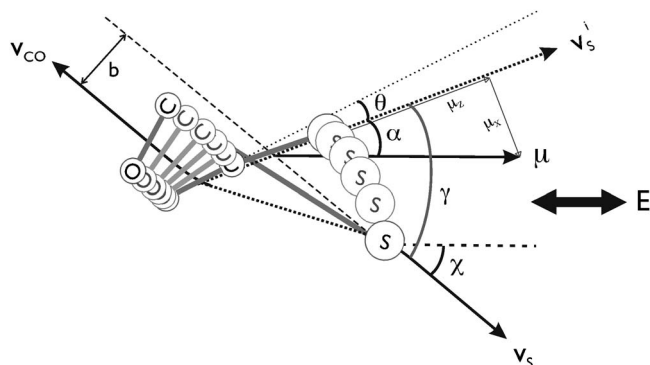


FIG. 8. Illustration for the geometry of OCS at the initial excitation to the $2^1A'$ excited state and during dissociation. α is the angle between the transition dipole moment (μ) and the initial recoil velocity (v_s) at Jacobi angle θ and χ can be measured from the experimental result (see the text for details).

moment in the molecular plane, schematically shown in Fig. 8. In this figure, the angle α between the transition dipole moment μ and the initial recoil direction is always in plane with the angle of rotation of the recoil axis γ . In this case, the parameter β can be presented as

$$\beta = 2P_2(\cos \chi), \quad (15)$$

where $\chi = \alpha + \gamma$ is the angle between the transition dipole moment μ and the recoil direction v_s in Fig. 8.

Equation (15), derived using a quantum mechanical approach, perfectly agrees with the result of classical treatment of the photodissociation of planar molecules.⁵⁶ According to the transition dipole moment calculation of Suzuki *et al.*, the angle between the transition dipole moment and the initial recoil direction is about -20° (α) at a Jacobi angle (θ) of $\sim 7^\circ$ for the single excitation to $2A'$ state. As mentioned previously, the transition dipole moment of the A' state does have a component in the molecular plane perpendicular to the recoil direction which could be the reason for showing a lower β than the limiting value of 2 even for pure axial recoil. The value of α might be changed during dissociation process depending on the change of the Jacobi angle. Using Eq. (15), the angle χ was determined from our experimental result ($\beta \approx 0.8$), giving $\chi \approx 39^\circ$. With the values of χ and α , the angle γ of $\sim 59^\circ$ is estimated. This suggests that the initial recoil velocity passes through μ by great bending and rotational motion of the parent molecule and ends at the final recoil direction with a certain transverse recoil angle. The comparison with the dissociation process at 230 nm, where the angle χ of $\sim 13^\circ$ was measured, implies that the larger deflection corresponding to the angle γ probably occurs at 193 nm rather than at 230 nm. In other words, a strong bending motion could be involved prior to C–S stretching at 193 nm to cause a larger deflection than in the 230 nm case.

Assuming dissociation from a parent molecule in $J=0$, the impact parameter (b) can readily be determined from the relative recoil velocity and rotational excitation in the CO fragment ($J=84$) using the well-known classical formula $L = \mu v b$. It is calculated to be about 1.4 \AA (shown in Fig. 8), which is smaller than that ($b \approx 2.4 \text{ \AA}$) at 230 nm photolysis. The large impact parameter associated with a high β value at

the longer wavelength is rather puzzling, and may reflect much lower impulsive recoil relative to bending motion than at 193 nm. However, this is difficult to reconcile with the χ values discussed above.

Given the present development of the theory, the terms containing the angle of rotation γ cannot be isolated from the expressions for the $K > 0$ anisotropy parameters for rotation of a planar molecule and therefore, the axial recoil anisotropy parameters cannot be determined. However, the general expressions in Eqs. (3)–(6) describing the experimental signals are still valid for the case of nonaxial recoil of a planar molecule if the anisotropy parameters s_k , α_k , γ_k , and η_k are assumed to be a function of γ . In this case, the alignment and orientation anisotropy parameters can still give us valuable insight into dissociation dynamics. The most important feature of the B ring is the obvious γ'_1 (coherent parallel and perpendicular excitations) contribution in that ring. It supports the view that dissociation in this region also involves excitation to the A'' state. As mentioned previously, the very different feature of γ_2 in the C ring indicates that fragments in the C ring might be produced via very different dynamics than those in the other rings. Furthermore, the smaller value of γ_2 relative to that in the A and B rings tells us that the coherent contribution is very small in the C ring. In other words, while the A and B rings are likely related to simultaneous excitations to both $2^1A'$ and $1^1A''$ states, the C ring is most likely to arise from single-surface ($2^1A'$) excitation. The observation of η corresponding to a coherent perpendicular dissociation mechanism possibly suggests a coherent superposition of the pure perpendicular transition to the $1^1A''$ state and the possible small perpendicular component of $2^1A'$ transition. However, it is less plausible to explain the η_4 alignment effect above the A ring with the same reason, since it is known experimentally and theoretically that the contribution from $1^1A''$ is associated with higher rotational levels than from $2^1A'$. The potential energy surface in the bent geometry (shown in Fig. 1) shows that there is another possible state ($2^1A''$) to be considered in the dissociation at the 193 nm case. Although the $2^1A''$ state has been ignored as out of reach ($\approx 6.2 \text{ eV}$) in earlier studies, at 193 nm (6.42 eV) it may be accessible, and the oscillator strength of this transition is almost the same as for the $1^1A''$ state. In addition, the fact that both $\eta_{2,4}$ in the C ring are nearly zero makes it more convincing that a nonadiabatic interaction following single-surface excitation is involved in the dissociation process.

For dissociation at 223 nm, the CO rotational distribution is peaked at $J=55$ and 67 for the faster and slower fragments, respectively.³⁷ Assuming that the efficiency of conversion of bending motion into CO rotation during the nonadiabatic transition is constant regardless of photolysis photon energy, one can easily expect $J=85$ for the slower fragments in our case. This simple argument makes it reasonable that S fragments in the C ring ($J=84$) may arise from dissociation initiated on the $2^1A'$ state followed by a nonadiabatic crossing to the ground state, which is also consistent with our interpretation for observed orientation and alignment parameters. All measured alignment and orientation parameters are summarized in Table II.

TABLE II. Measured alignment and orientation parameters for $S(^1D_2)$ from 193 nm dissociation of OCS.

Parameter	Region C	Region B ^a	Region A ^a
β	0.8	0.3	0.4
α_1	0.00	0.01	0.01
γ_1	0.02	0.00	-0.02
γ'_1	0.01	-0.04	0.02
s_2	-0.03	-0.06	-0.06
α_2	0.08	0.05	0.04
γ_2	-0.02	0.05	0.06
η_2	0.01	0.03	0.02
s_4		-0.04	-0.06
α_4		-0.03	0.03
γ_4		0.03	0.04
η_4		-0.09	-0.11

^aReported rank 4 anisotropy parameters are obtained at ~ 50 m/s faster velocity region.

As mentioned previously, wave packet calculations showed three distinct rotational distributions. Although the contributions of two adiabatic pathways via each $2^1A'$ or A'' state were not resolved experimentally at ~ 230 nm photolysis, it is perhaps not surprising that the separation in energy between two pathways is clearer in the present results, both owing to the higher resolution of dc slice imaging and the greater available energy following 193 nm dissociation. Our results also suggest that the nonadiabatic transition (peak C) has a stronger contribution relative to other dissociation dynamics processes at 193 nm in contrast with previous results at the longer photolysis wavelengths. It is known that the probability of nonadiabatic crossing is larger as the photolysis energy increases owing to the greater possibility for reaching the $1^1A''$ excited state which lies higher in energy than the $1^1A'$ state. In addition, the Landau-Zener picture can also account for the larger probability of nonadiabatic crossing is proportional to the recoil velocity and the difference in slopes of the two diabatic potential surfaces at the crossing point. The recoil speed of the S fragments at the nonadiabatic avoided crossing region is about 1150 m/s, which is faster than that (~ 780 m/s) at 223 nm by *et al.*³⁷ That is, the diabatic pathway is more probable than the adiabatic pathway at the shorter wavelength, which could be reflected in the increased signal level in the C ring.

Some features in the D region show resolved rotational structure of CO as described in Sec. IV. The energy spacing of well-separated rings (~ 0.028 eV) gives us a hint for rotational states of CO in this region. Using the rotational constant (B_0) and vibration-rotation interaction constant (α), we estimated a vibrationally dependent rotation constant to assign those rings to $J=63$ –64 rotational levels in $v=4$ excited vibrational state. The structure in the D region thus implies that some contribution of highly vibrationally excited CO cofragments possibly underlies the main rings of CO in the ground vibrational state. Although most results of OCS photodissociation at 223 nm and longer wavelength report that the vibrational excitation of CO is negligible,^{37,57} it appears

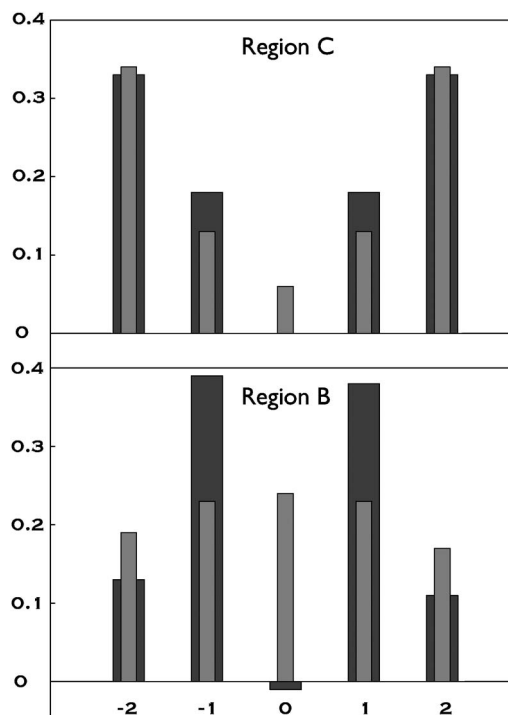


FIG. 9. The population of each magnetic sublevel for $S(^1D_2)$ atom at the recoil angle of 0° for the fragments in region C (top) and region B (bottom). The wide darker bar corresponds to the complete density matrix, and the narrow lighter bar indicates the density matrix calculated excluding the rank 4 contributions. The uncertainty in the determination of these populations is typically less than ± 0.04 based on reproducibility over several measurements.

that some vibrationally excited CO are produced at 193 nm, given much greater available energy and possible access to other excited states.

A thorough analysis of angular momentum polarization allows us to construct the full molecular frame sulfur atom density matrix, including explicitly the relative population of each magnetic sublevel and the coherences embodied in the off-diagonal elements. The full density matrix in the molecular frame calculated using all measured anisotropy parameters are reported here for recoil angles of 0° , 45° , and 90° in the circularly polarized dissociation light case. Figure 9 displays the diagonal elements of density matrices for the photofragments in the C and B rings recoiling along the polarization of photolysis light. In the C ring, it is apparent that \mathbf{v} is parallel to \mathbf{J} for either case with or without the higher order $K=4$ contributions. On the other hand, for the density matrix in the B ring these are surprisingly different from one another. This means that the hexadecapole moment ($K=4$) of the angular momentum distribution is particularly important in this recoil region and must be considered to obtain the complete density matrix accurately. The distribution of the $|m_J|$ population is peaked at $|m_J|=1$ with an additional small orientation toward the $m_J=-1$ level. It is noted that there is a physically impossible negative element in the $m_J=0$ sublevel, implying that the rank 4 contributions might be slightly overestimated. For the B ring, the full density matrices for recoil angles of 45° and 90° including all rank $K=0$ –4 contributions are

$$\rho_{m'm}^{45^\circ} = \begin{pmatrix} 0.10 & -0.05(-0.01) & -0.03 & 0 & 0 \\ -0.05(0.01) & 0.34 & 0.02(-0.01) & 0.07 & 0 \\ -0.03 & 0.02(0.01) & 0.15 & -0.02(-0.01) & -0.03 \\ 0 & 0.07 & -0.02(0.01) & 0.34 & 0.05(-0.01) \\ 0 & 0 & -0.03 & 0.05(0.01) & 0.08 \end{pmatrix},$$

$$\rho_{m'm}^{90^\circ} = \begin{pmatrix} 0.06 & 0.00(0.00) & -0.05 & 0 & 0 \\ 0.00(0.00) & 0.30 & 0.00(0.00) & 0.13 & 0 \\ -0.05 & 0.00(0.00) & 0.27 & 0.00(0.00) & -0.05 \\ 0 & 0.13 & 0.00(0.00) & 0.30 & 0.00(0.00) \\ 0 & 0 & -0.05 & 0.00(0.00) & 0.06 \end{pmatrix},$$

where the values in parentheses refer to an imaginary part of the coherence which mostly comes from the γ_1' contribution. The nonzero off-diagonal terms indicate the coherent interactions present in this system. The uncertainty in the determination of these matrix elements is typically better than ± 0.04 for the diagonal elements and ± 0.01 for the off-diagonal terms based on reproducibility over several independent measurements.

VI. CONCLUSION

We have measured all possible alignment and orientation of $S(^1D_2)$ arising from the dissociation of OCS at 193 nm using dc sliced imaging. Three peaks corresponding to specific groups of high rotational levels of CO in the vibrational ground state are shown, with the rotationally resolved rings at the D region ascribed to weak signals associated with excited vibrational states of CO. The observed speed-dependent β parameter and coherent alignment or orientation support that there are two main dissociation processes: the simultaneous two-surface (A' and A'') excitation and the initial single-surface (A') excitation followed by the nonadiabatic crossing to ground state. At 193 nm photodissociation, the nonadiabatic dissociation process is strongly enhanced relative to longer wavelengths. This can be ascribed to the increased probability of the nonadiabatic transition by the faster-speed fragments and greater contribution of excitation to the A' state, compared to those at the lower photolysis energy case. Furthermore, the dissociation happens via non-axial recoil dynamics due to the larger deflection associated with a bending motion of parent OCS molecule during dissociation.

The complete density matrix was constructed including the higher order ($K=3,4$) contributions for the circularly polarized dissociation light. It reveals the $\mathbf{v} \parallel \mathbf{J}$ correlation in the S atom at the C ring and the preferential population of $|m_J|=1$ at the B ring, respectively. In particular, it was found that the density matrix in the B ring is sensitively affected by the rank 4 terms. This suggests that the higher order contributions should not be overlooked to understand deeply the underlying dissociation dynamics in this system.

ACKNOWLEDGMENTS

The authors would like to acknowledge Dr. W. Li for his help with refining the imaging acquisition program for our experimental setup and L. Shen for calculations. This work was supported by the National Science Foundation under Award No CHE-0415393.

- ¹R. J. Van Brunt and R. N. Zare, J. Chem. Phys. **48**, 4304 (1968).
- ²Y. Mo, H. Katayanagi, M. C. Heaven, and T. Suzuki, Phys. Rev. Lett. **77**, 830 (1996).
- ³A. T. J. B. Eppink, D. H. Parker, M. H. M. Janssen, B. Buijsse, and W. J. van der Zande, J. Chem. Phys. **108**, 1305 (1998).
- ⁴A. S. Bracker, E. R. Wouters, A. G. Suits, and O. S. Vasyutinskii, J. Chem. Phys. **110**, 6749 (1999).
- ⁵Y. Wang, H. P. Looock, J. Cao, and C. X. W. Qian, J. Chem. Phys. **102**, 808 (1995).
- ⁶T. P. Rakitzis, S. A. Kandel, and R. N. Zare, J. Chem. Phys. **108**, 8291 (1998).
- ⁷S. W. North, X. S. Zheng, R. Fei, and G. E. Hall, J. Chem. Phys. **104**, 2129 (1996).
- ⁸M. L. Costen, S. W. North, and G. E. Hall, J. Chem. Phys. **111**, 6735 (1999).
- ⁹E. R. Wouters, M. Ahmed, D. S. Peterka, A. S. Bracker, A. G. Suits, and O. S. Vasyutinskii, in *Imaging in Chemical Dynamics*, edited by R. E. Continetti and A. G. Suits (American Chemical Society, Washington, 2000), p. 238.
- ¹⁰A. G. Smolin, O. S. Vasyutinskii, O. P. J. Vieuxmaire, M. N. R. Ashfold, G. G. Balint-Kurt, and A. J. Orr-Ewing, J. Chem. Phys. **124**, 094305 (2006).
- ¹¹A. G. Smolin, O. S. Vasyutinskii, E. R. Wouters, and A. G. Suits, J. Chem. Phys. **121**, 6759 (2004).
- ¹²C. R. Gebhardt, T. P. Rakitzis, P. C. Samartzis, V. Ladopoulos, and T. N. Kitsopoulos, Rev. Sci. Instrum. **72**, 3848 (2001).
- ¹³D. Townsend, M. P. Minitti, and A. G. Suits, Rev. Sci. Instrum. **74**, 2530 (2003).
- ¹⁴J. J. Lin, J. Zhou, W. Shiu, and K. Liu, Rev. Sci. Instrum. **74**, 2495 (2003).
- ¹⁵D. Townsend, S. K. Lee, and A. G. Suits, Chem. Phys. **301**, 197 (2004).
- ¹⁶S. K. Lee, D. Townsend, O. S. Vasyutinskii, and A. G. Suits, Phys. Chem. Chem. Phys. **7**, 1650 (2005).
- ¹⁷M. J. Bass, M. Brouard, A. P. Clark, C. Vallance, and B. Martinez-Haya, Phys. Chem. Chem. Phys. **5**, 856 (2003).
- ¹⁸M. Ahmed, D. S. Peterka, A. S. Bracker, O. S. Vasyutinskii, and A. G. Suits, J. Chem. Phys. **110**, 4115 (1999).
- ¹⁹M. Ahmed, E. R. Wouters, D. S. Peterka, O. S. Vasyutinskii, and A. G. Suits, Faraday Discuss. **113**, 425 (1999).
- ²⁰M. Brouard, A. P. Clark, C. Vallance, and O. S. Vasyutinskii, J. Chem. Phys. **119**, 771 (2003).
- ²¹T. M. Teule, G. C. Groenenboom, D. W. Neyer, D. W. Chandler, and M. H. M. Janssen, Chem. Phys. Lett. **320**, 177 (2000).

- ²²E. R. Wouters, M. Beckert, L. J. Russell, K. N. Rosser, A. J. Orr-Ewing, M. N. R. Ashfold, and O. S. Vasyutinskii, *J. Chem. Phys.* **117**, 2087 (2002).
- ²³S. M. Dylewski, J. D. Geiser, and P. L. Houston, *J. Chem. Phys.* **115**, 7460 (2001).
- ²⁴T. P. Rakitzis, P. C. Samartzis, and T. N. Kitsopoulos, *Phys. Rev. Lett.* **87**, 123001 (2001).
- ²⁵T. P. Rakitzis, R. L. Toomes, L. Tsigaridas, M. Coriou, D. Chestakov, A. T. J. B. Eppink, D. H. Parker, and T. N. Kitsopoulos, *Chem. Phys. Lett.* **364**, 115 (2002).
- ²⁶T. P. Rakitzis, P. C. Samartzis, R. L. Toomes, and T. N. Kitsopoulos, *J. Chem. Phys.* **121**, 7222 (2004).
- ²⁷M. Brouard, R. Cireasa, A. P. Clark, T. J. Preston, C. Vallance, G. C. Groenenboom, and O. S. Vasyutinskii, *J. Phys. Chem. A* **108**, 7965 (2004).
- ²⁸A. J. Alexander and R. N. Zare, *Acc. Chem. Res.* **33**, 199 (2000).
- ²⁹T. P. Rakitzis, S. A. Kandel, A. J. Alexander, Z. H. Kim, and R. N. Zare, *Science* **281**, 1346 (1998).
- ³⁰T. P. Rakitzis, P. C. Samartzis, R. L. Toomes, T. N. Kitsopoulos, A. Brown, G. G. Balint-Kurti, O. S. Vasyutinskii, and J. A. Beswick, *Science* **300**, 1936 (2003).
- ³¹T. P. Rakitzis, P. C. Samartzis, and T. N. Kitsopoulos, *J. Chem. Phys.* **111**, 10415 (1999).
- ³²A. J. van den Brom, T. P. Rakitzis, and M. H. M. Janssen, *J. Chem. Phys.* **123**, 164313 (2005).
- ³³Z. H. Kim, A. J. Alexander, and R. N. Zare, *J. Phys. Chem. A* **103**, 10144 (1999).
- ³⁴D. Townsend, W. Li, S. K. Lee, R. L. Gross, and A. G. Suits, *J. Phys. Chem. A* **109**, 8661 (2005).
- ³⁵J. C. Polanyi and P. A. Young, *J. Chem. Phys.* **93**, 3673 (1990).
- ³⁶W. Kedzierski, J. Borbely, and J. W. McConkey, *J. Phys. B* **34**, 4027 (2001).
- ³⁷T. Suzuki, H. Katayanagi, S. Nanbu, and M. Aoyagi, *J. Chem. Phys.* **109**, 5778 (1998).
- ³⁸H. Katayanagi and T. Suzuki, *Chem. Phys. Lett.* **360**, 104 (2002).
- ³⁹A. Sugita, M. Mashino, M. Kawasaki, Y. Matsumi, R. Bersohn, G. Trott-Kriegeskorte, and K. H. Gericke, *J. Chem. Phys.* **112**, 7095 (2000).
- ⁴⁰A. M. Rijs, E. H. G. Backus, C. A. de Lange, M. H. M. Janssen, N. P. C. Westwood, K. Wang, and V. McKoy, *J. Chem. Phys.* **116**, 2776 (2002).
- ⁴¹A. J. van den Brom, T. P. Rakitzis, J. van Heyst, T. N. Kitsopoulos, and M. H. M. Janssen, *J. Chem. Phys.* **117**, 4255 (2002).
- ⁴²C. E. Strauss, G. C. McBane, P. L. Houston, I. Burak, and J. W. Hepburn, *J. Chem. Phys.* **90**, 5364 (1989).
- ⁴³S. M. Wu, X. Yang, and D. H. Parker, *Mol. Phys.* **103**, 1797 (2005).
- ⁴⁴M. H. Kim, W. Li, S. K. Lee, and A. G. Suits, *Can. J. Chem.* **82**, 880 (2004).
- ⁴⁵W. Li, S. D. Chambreau, S. A. Lahankar, and A. G. Suits, *Rev. Sci. Instrum.* **76**, 063106 (2005).
- ⁴⁶A. C. Kummel, G. O. Sitz, and R. N. Zare, *J. Chem. Phys.* **85**, 6874 (1986).
- ⁴⁷A. C. Kummel, G. O. Sitz, and R. N. Zare, *J. Chem. Phys.* **88**, 6707 (1987).
- ⁴⁸Y. Mo and T. Suzuki, *J. Chem. Phys.* **109**, 4691 (1998).
- ⁴⁹B. V. Pichayev, A. G. Smolin, and O. S. Vasyutinskii, *J. Phys. Chem.* **101**, 7614 (1997).
- ⁵⁰L. D. A. Siebbeles, M. Glass-Maujean, O. S. Vasyutinskii, J. A. Beswick, and O. Roncero, *J. Chem. Phys.* **100**, 3610 (1994).
- ⁵¹A. G. Suits and O. S. Vasyutinskii (unpublished).
- ⁵²K. Blum, *Density Matrix Theory and Application* (Plenum, New York, 1996).
- ⁵³R. N. Zare, *Angular Momentum* (Wiley, New York, 1988).
- ⁵⁴T. P. Rakitzis, A. J. van den Brom, and M. H. M. Janssen, *Science* **303**, 1852 (2004).
- ⁵⁵V. V. Kuznetsov and O. S. Vasyutinskii, *J. Chem. Phys.* **123**, 34307 (2005).
- ⁵⁶A. V. Demyanenko, V. Dribinski, H. Reisler, H. Meyer, and C. X. W. Qian, *J. Chem. Phys.* **111**, 7383 (1999).
- ⁵⁷N. Sivakumar, G. E. Hall, P. L. Houston, J. W. Hepburn, and I. Burak, *J. Chem. Phys.* **88**, 3692 (1988).